applied sciences

MDPI

Article

High-Performance Asymmetric Supercapacitors Based on the Surfactant/Ionic Liquid Complex Intercalated Reduced Graphene Oxide Composites

Jun-Hong Lin *, Bo-Wen Shi and Zhao-Cheng Chen

Department of Mold and Die Engineering, National Kaohsiung University of Applied Sciences, Kaohsiung 807, Taiwan; sevennater@gmail.com (B.-W.S.); kuasmd401@gmail.com (Z.-C.C.)

* Correspondence: jhlin@kuas.edu.tw; Tel.: +886-7-38-145-265-426

Received: 24 January 2018; Accepted: 20 March 2018; Published: 23 March 2018

Abstract: In this paper, ionic surfactants are employed to intercalate thermally-reduced graphene oxide (TRG). The ionic interaction between the intercalated surfactant and the ionic liquid could lead to the formation of large-sized ionic aggregates and, hence, enlarge the interlayer distance between the TRG sheets. The morphology and vibration modes of these composites were systematically characterized using XRD (X-ray diffraction), SAXS (small-angle X-ray scattering), and FTIR (Fourier transform infrared spectroscopy). An asymmetric supercapacitor, which consisted of a cationic surfactant-intercalated electrode on one side and an anionic surfactant-intercalated electrode on the other, was examined. It was found that, with the increased interlayer distance, the energy density and capacitance of the cells were improved. It seems that the cell with a cationic surfactant as the cathode had the best energy density of 67.8 Wh/kg, which is 4.4-fold higher than that of the TRG cell.

Keywords: supercapacitors; reduced graphene oxide; asymmetric electrode; ionic liquids

1. Introduction

With the growing concerns regarding climate change and the depletion of fossil fuels, researchers have paid a great deal of attention towards developing high-performance energy storage devices. As an energy device, supercapacitors have drawn a great deal of interest from the point of view of research and applications because of their merits—their high power density, excellent efficiency, wide range of operation temperatures, long cycle life, and requiring very little maintenance [1,2]. One type of a supercapacitor, called the electrical double layer capacitor (EDLC), stores energy in an electrical double layer through fast ion adsorption and desorption process at the interface between the electrolyte and electrode. Therefore, it would be vital to obtain an understanding of the charge dynamics of the ions, in both the electrode and electrolyte [3]. Our earlier investigations on the charge dynamics of ionic liquid between two electrodes reveal that, during the charging process, the mobile ions that participate in energy storage are mainly from the region near the electrode, rather than from the bulk of the electrolyte [4,5]. Furthermore, the charging of the electrode is a combination effect of both the attractive and repulsive interactions, depending on the polarity of the ions [4,6]. Therefore, the ionic species intercalated on, or near, the electrode would play an essential role in the performance of EDLC.

However, based on the physical relation, the energy density is $E = 0.5\ CV^2$, where C is the capacitance of the cell related to the surface area of the electrode and V is the applied voltage. Therefore, the improvements in EDLC cells are centered on developing highly conductive porous materials, discovering electrolytes with wide electrochemical windows and modifying the electrode/electrolyte interface properties. For high-performance electrolytes, a particular group of molten salts, called ionic liquids (ILs), are becoming favorable for EDLC applications. ILs possess qualities including

high conductivity, a wide electrochemical window, low viscosity, low volatility and a capacity for high stability at high temperatures [7,8]. However, ILs comprise of both cations and anions, and the size of these comprising ions could be large, which may hinder the ability of ILs regarding accessing small pores.

On the other hand, reduced graphene oxide (RGO) is a promising high specific surface area materials for ion storage because of its high electrical conductivity and large, theoretical, specific surface area (2630 m^2/g). Since graphene oxide (GO) can be obtained by the chemical oxidation of natural graphite particles, RGO has the potential to be mass produced [9,10]. GO is an amphiphile as a result of the defects and the attached hydrophilic oxygen groups that are introduced to the hydrophobic basal plane of graphene during the oxidation process. These attached hydrophilic oxygen functional groups could isolate the electrical conduction between GO particles and could disperse the GO as a few layers of sheets in water [11], whereas the thermal reduction process, provides an easy way for converting GO into thermally-reduced graphene oxides (TRG) by removing the attached oxygen groups at elevated temperatures. Without the use of strong chemical bases, it is a chemically free and environmentally-friendly process [12,13]. However, without the oxygen groups, the hydrophobic nature of TRG is almost water insoluble, thus hampering further processing of the material composites [11]. In the existing literature, ionic surfactants are often utilized to stabilize RGO suspensions in water and avoid the restacking of RGO in a solid form [14,15]. Ionic surfactants are amphiphilic compounds because they are composed of ionic hydrophilic head groups and extended apolar, hydrophobic tails. Thus, the surfactant can interact with the RGO surfactant through the static forces between the charged head groups and the residual oxygen groups. In addition, the hydrophobic interactions between the aliphatic chains and hydrophobic basal planes are essential in the stabilization of individual RGO sheets in water [14].

Zhang et al. [15] employed a series of ionic surfactants to stabilize the GO sheets during the reduction process. They found that the surfactants successfully intercalated in both the GO and the RGO sheets, preventing the restacking phenomena. In addition, their results indicated that the aqueous electrolytes had a higher capacitance response than the ILs electrolytes for the same surfactant intercalated electrodes. This may be due to the fact that aqueous electrolytes usually have small ions that, therefore, facilitated ion transport in small pores [16]. In contrast, for example, the average ion diameter of 1-ethyl-3-methylimidazolium bis(trifluoromethylsulfonyl)imide, (EMI-TFSI) is D~0.7 nm [17], which is usually larger than the reported interlayer distance of surfactant intercalated RGO (~0.4 nm). Thus, the small interlayer distance may have prohibited the IL to access the surface area in between the RGO sheets. Here, we propose a facile approach to enlarge the interlayer distance with the assistance of an anionic surfactant, Sodium dodecyl sulfate (SDS), or a cationic surfactant, Cetyltrimethylammonium bromide (CTAB), shown in Figure 1. SDS consists of a 12-carbon tail with a negatively-charged head group (SO_4^-) and a sodium counter ion (Na^+). In contrast, CTAB consists of a 16-carbon tail with a positively-charged head group (N-$(CH_3)_3^+$) and a bromide counterion (Br^-) [15]. The anionic surfactant, SDS, was intercalated in between the TRG sheets, forming a composite named TRGS. Afterward, these intercalated TRGS sheets were rinsed with an EMI-TFSI solution during filtration and was named as TRGSE (Thermally reduced graphene oxide intercalated with SDS and EMI-TFSI). Following the same procedures and using the cationic surfactant CTAB, TRGCE (Thermally reduced graphene oxide intercalated with CTAB and EMI-TFSI) composites could be obtained. The Coulombic force between the ILs and the intercalated ionic surfactants may have led to large-sized ionic aggregates or micelles and, thus, increased the interlayer distance. Additionally, the asymmetric EDLC cell, which is composed of TRGCE on one side and TRGSE on the other side, allowed us to investigate the intercalated ion species on the performance of the cell under different polarities of charging voltages. For example, the cell with TRGSE as the cathode and TRGCE as an anode was named as S+C−, while the cell with TRGSE as the anode and TREGCE as the cathode was named S−C+, as shown in Figure 2. Additionally, an EDLC cell with neat TRG as the electrode was prepared for comparison.

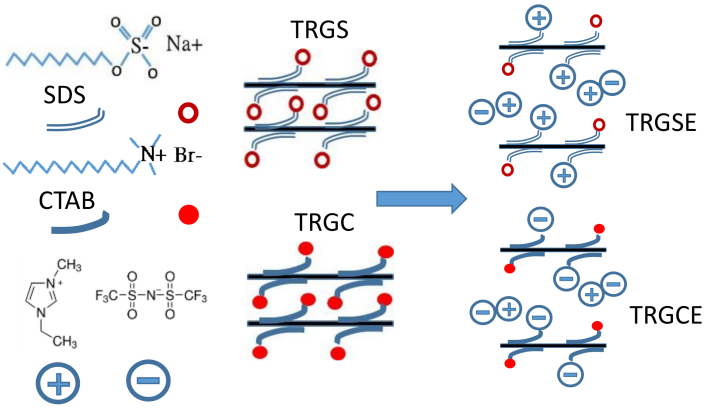

Figure 1. The depiction of the process to enlarge the interlayer distance between TRG sheets through the Coulombic force interaction. TRG: thermally-reduced graphene oxides; SDS: Sodium dodecyl sulfate; CTAB: Cetyltrimethylammonium bromide; TRGS: Thermally reduced graphene oxide intercalated with SDS; TRGC: Thermally reduced graphene oxide intercalated with CTAB; TRGSE: Thermally reduced graphene oxide intercalated with SDS and EMI-TFSI; TRGCE: Thermally reduced graphene oxide intercalated with CTAB and EMI-TFSI.

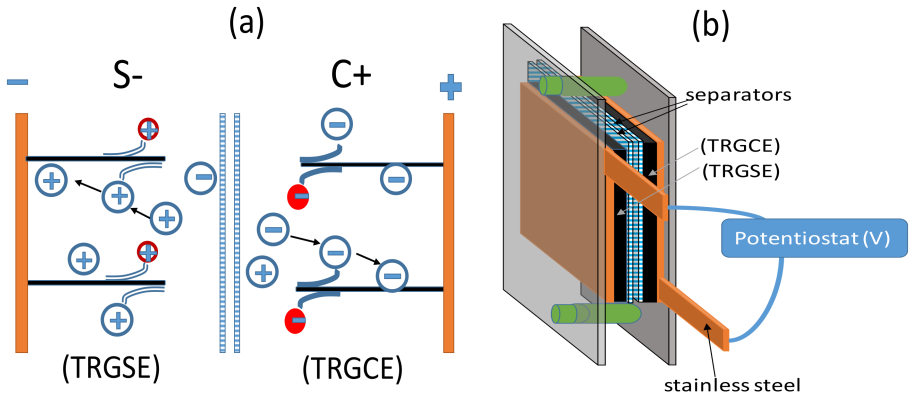

Figure 2. Schematic of (**a**) the structure of the S−C+ EDLC (electrical double layer capacitor) cell and (**b**) the supercapacitor cell for electrical measurement.

2. Materials and Methods

The thermally-reduce graphene oxide (TRG) was purchased from the GIBusiness, Taiwan, and was synthesized from natural graphite using a modified Hummers method [18], followed by thermal treatment at elevated temperatures. Typically, 10 mg of TRG powder was dispersed in 30 mL of 0.1 M CTAB surfactant solution with the aid of ultrasonication and vigorous stirring for 12 h. After that, 3 mL of the mixture containing 1 mg of TRG was deposited on a 1 cm^2 Celgard 3500 separator using a vacuum filter to obtain the TRGC electrodes. Furthermore, the TRGC electrodes were rinsed with 1.5 mL of 0.2 M of EMI-TFSI ethanol solution during filtration to obtain the TRGCE electrodes. The filtrated electrode on the separator was flipped over on a 1 cm^2 of 0.1 mm thick 304 stainless steel current collector to prepare each side of the electrode as shown in Figure 2b. The TRGSE samples were obtained following the same procedure but using SDS as surfactant. The EDLC cell was in the form of a two-electrode package inside a sealed polypropylene testing bag, filled with EMI-TFSI as the electrolyte as shown in Figure 2. For comparison, the TRG electrodes were also produced by dispersing 10 mg of TRG in 30 mL of 20 wt % of ethanol solution using the same dispersion and filtration process. The electrical impedance spectroscopy (EIS, 0.1 to 1 MHz), cyclic voltammetry (CV, between 0 and 3.2 V), and galvanostatic charging and discharging (between 0 and 3.2 V) measurements were made using a potentiostat (potentiostat, VersaSTAT 4, Princeton Applied Research, Oak Ridge,

TN, USA) using the two-electrode method. The microstructures of the composites were characterized via a scanning electron microscope (SEM, JEOL 6700, 5 kV, Tokyo, Japan), X-ray diffraction (XRD; Bruker-AXS D8, CuKα = 1.5406 Å, Karlsruhe, Germany), and small angle X-ray (SAXS, Nanostar U system, Bruker AXS Gmbh, CuKα = 1.5406 Å, Karlsruhe, Germany). The weight composition was determined by thermal gravimetric analyses (TGA; TAQ50, TA Instruments, New Castle, DE, USA) at a heating rate of 10 °C /min under nitrogen flow). A Fourier Transform Infrared Spectrometer (FTIR, Bruker Vertex 70v, Ettlingen, Germany) was also used to investigate the bond vibration in a wave number range of 4000 to 400 cm^{-1}.

3. Results

The SEM images of the TRG, TRGSE, and TRGCE were shown in Figure 3. As can be seen, without surfactant intercalation, TRG would tend to agglomerate into graphite-like large particles. In contrast, the TRGSE and TRGCE seem to appear more curved and crumbly in their primary structures, with more irregular wrinkled edges, implying the intercalation of the surfactants/ionic liquid complex that efficiently separates the TRG into a few layers structures.

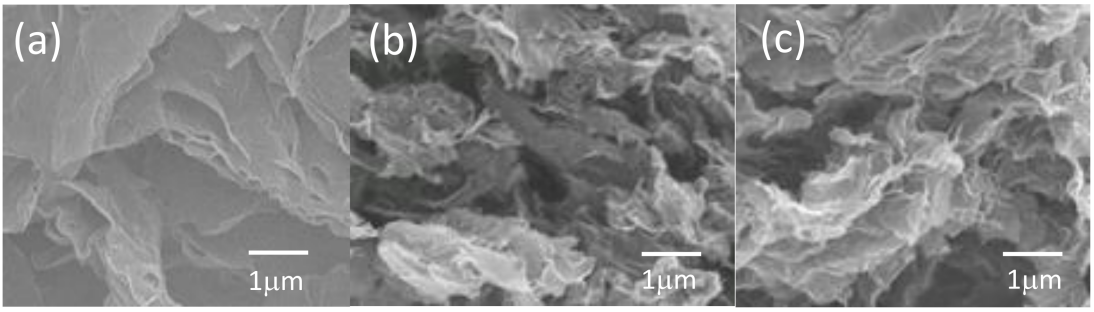

Figure 3. The SEM (scanning electron microscope) image of (**a**) TRG, (**b**) TRGSE, and (**c**) TRGCE.

Figure 4 plots the Fourier Transform Infrared Spectrometer (FTIR) spectroscopy for neat TRG, TRGS, TRGSE, TRGC, and TRGCE in the wavenumber region of 4000–400 cm^{-1}. In the existing literature, several characteristic vibration modes corresponding to GO's specific functional groups are often reported, including those in a lower frequency region, with bands at 1033 cm^{-1} and 1154 cm^{-1}, representing the stretching modes of C-O, and C-OH, respectively. While in a higher frequency region, the bands at 3430 cm^{-1}, 1716 cm^{-1} and 1635 cm^{-1} correspond to the stretching mode of O-H, C=O, and C=C, respectively. As shown in Figure 4a, for the TRG sample, most of the oxygen-related groups were markedly removed, leaving two small broad peaks at 1154 cm^{-1} and 3430 cm^{-1}, which corresponded to some residual C-OH and O-H groups, respectively. In the TRGSE spectrum, the bands related to the C-H vibration of the intercalated SDS at bands 2955 cm^{-1},2917 cm^{-1} and 2849 cm^{-1} were not affected by EMI-FSI. However, the bands at 1219 cm^{-1} and 1249 cm^{-1}, which corresponded to the SO_2 asymmetric vibration [19,20], were found to have shifted to 1226 cm^{-1} and disappeared, respectively. These strong shifts may imply the Coulombic force or the ion exchange interaction between the intercalated SDS and the EMI-TFSI in the TRGSE samples. Similarly, in the TRGCE spectrum, the bands related to the C-H bond vibration of the intercalated CTAB at 2917 cm^{-1} and 2849 cm^{-1} were not affected by the EMI-FSI. Nevertheless, the band at 2958 cm^{-1}, which represented the symmetric stretching of the N-CH_3 vibration [19,20], was found to have dramatically shifted to 2969 cm^{-1}. This substantial shift in the head group of intercalated CTAB may prove a Coulombic interaction or ion exchange between intercalated CTAB and EMI-TFSI.

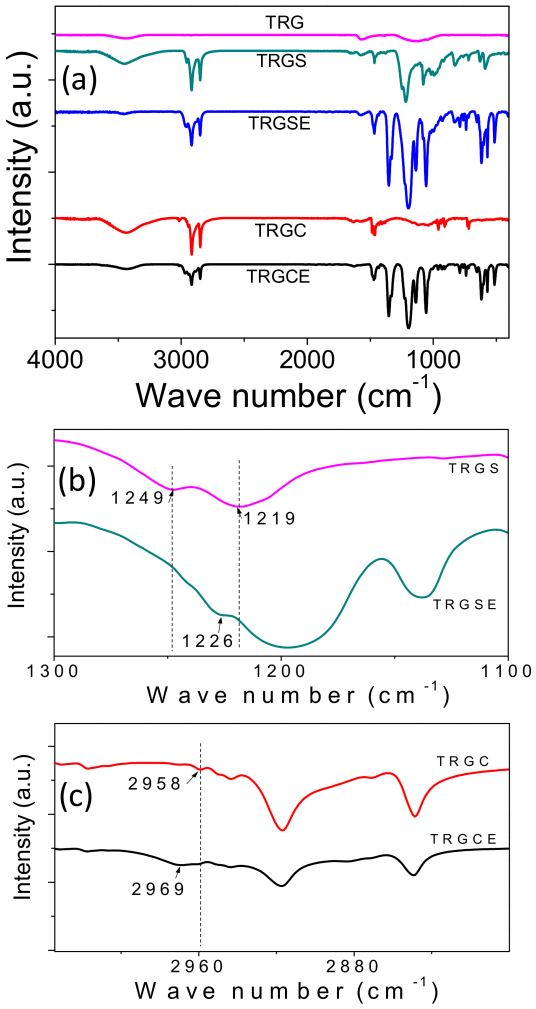

Figure 4. (**a**) FTIR (Fourier Transform infrared spectroscopy) spectra of TRG, TRGS, TRGSE, TRGC, and TRGCE; (**b**,**c**) a magnified image for the specific wavenumber region.

Figure 5 plots the thermal gravimetric analysis (TGA) results, showing the retained weight vs. temperature of the neat TRG, TRGSE and TRGCE composites. It appears that all the composites showed a little mass loss at around 100 °C due to moisture content. The TRG displayed a smooth weight loss from 100 to 500 °C with an 8% total weight loss at 500 °C, followed by a steep weight loss due to the quick decomposition of TRG. On the other hand, TRGSE and TRGCE show steep weight losses at around 200 °C due to the decomposition of SDS, CTAB, and EMI-TFSI between the TRG sheets. The weight losses of 17% and 28% at 500 °C were observed for the TRGCE and the TRGSE samples, respectively. Compared to TRG, the additional weight loss of the TRGCE and TRGSE might be due to the intercalated CTAB/EMI-TFSI and SDS/EMI-TFSI complexes, accordingly.

The specific feature structures of TRG, TRGCE, and TRGSE were revealed by X-ray diffraction (XRD) and small angle X-ray scattering (SAXS) measurements. Figure 6a displays the X-ray intensity versus the scattering angle 2θ. As can be seen, the XRD pattern for TRG shows (001) reflection peak at 24.6 degrees, corresponding to the average interlayer distance of 0.36 nm, which is consistent with the reported results [15]. TRGCE shows the (001) main peak at 21.5 degrees and a minor peak at 12.4, corresponding to interlayer distances of 0.41 nm and 0.71 nm, respectively. While TRGSE exhibits a (001) reflection peak mainly at 13.3 degrees, representing an interlayer distance of 0.67 nm. It seems that both TRGCE and TRGSE have more than one reflection peak. Therefore, the interlayer distance of the composites should depend on the morphology of the intercalated species. To confirm the existence

of more considerable interlayer distances of these composites, SAXS measurements were carried out. SAXS probes the repeating microfeatures in a distance range between a few nm to a few tens of nm in polymers or their composites. Figure 6b presents the SAXS patterns obtained from TRG, TRGCE, and TRGSE, which were expressed as scattering intensity vs. q and corrected for background scattering. The repeating structures of different shapes and sizes can be determined using the scattering vector $q = \frac{4\pi sin\theta}{\lambda}$ in the equation $d = \frac{2\pi}{q}$ [21]. As can be seen in Figure 6b, in the low q region, the increase in the power law decay exponent represents the scattering of larger-sized objects [21]. For the TRG sample, no specific peak was observed over the whole measured region, implying that no repeating features in the distance range of SAXS were detected. As can be seen, TRGCE showed a scattering peak at q = 0.25 A^{-1}, representing an interlayer distance of 2.51 nm, whereas TRGSE exhibited a sharp scattering peak at q = 0.16 A^{-1} indicating an interlayer distance of 3.92 nm. These results indicated that the interlayer distances of both TRGCE and TRGSE are much greater than that of the TRG, suggesting the formation of sizeable ionic aggregation or micelles between the TRG sheets.

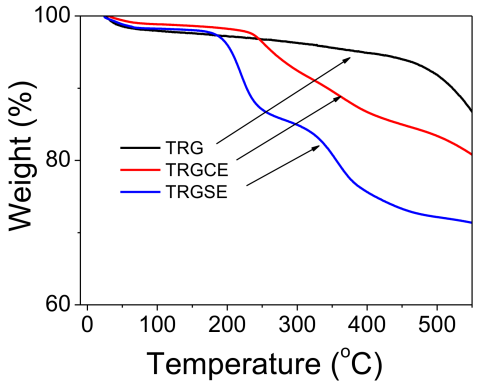

Figure 5. The thermal gravimetric analysis for the TRG, TRGCE and TRGSE samples.

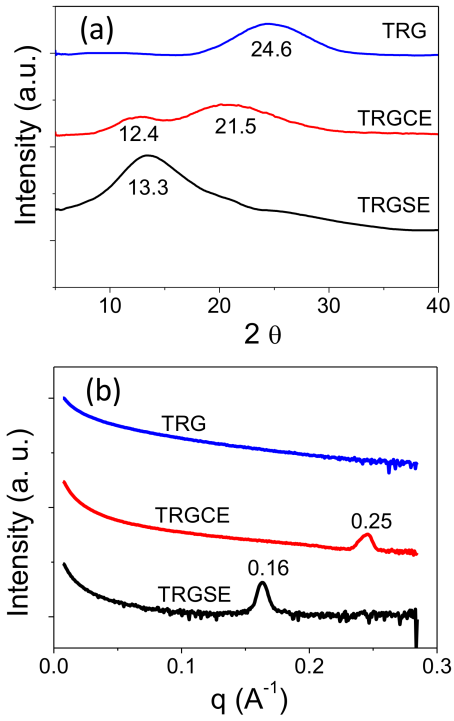

Figure 6. (**a**) X-ray diffraction scattering and (**b**) small angle X-ray scattering of the TRG, TRGCE and TRGSE composites.

In this experiment, the asymmetrical structure of a two-electrode EDLC cell (Figure 2) comprised of a TRGSE electrode on one side and TRGCE on the other. Figure 7 shows a Nyquist plot for the TRG, TRGCE and TRGSE cells where the image part of the impedance was plotted against the real part of the impedance. The AC (alternating current) impedance measurement was carried out by applying an AC signal (100 mV) from 1 M Hz to 0.1 Hz. For example, from high to low frequency, the impedance curve of the S−C+ cell showed a semicircle, followed by a transition zone transferringto a vertical line. As can be seen, the semicircle intercepted or approached the real axis at Rs and Rs + Rc. Rs is usually related to the resistance of ion transport in an electrolyte. In a highly-conductive electrolyte, Rc is mainly attributed to electron conduction in the cells, including the contact resistance between conductive composite particles and that between the composite electrodes and the current collectors [22,23]. The high- to medium-frequency region denotes the ion transfer resistance associated with the porous structure of the electrodes in the S−C+ cell. Due to the ion diffusion mechanism of the S−C+ cell between the Warburg diffusion and the ideal capacitive ion diffusion [22,24], the impedance response deviated from the vertical line to an inclined angle between 45° and 90° against the real axis (inset of Figure 7). This non-ideal capacitance response can be attributed to the pore size distribution, which induced a different penetration depth of the S−C+ cell [24]. The resistance Rp represents the Warburg-related diffusion process in the S−C+ cell, which can be approximately deduced by extrapolating the low-frequency data to the real axis. The x-axis intercept is, therefore, equal to the internal resistance R = Rs + Rc + Rp [25,26] (Figure 7, inset). All the samples shared similar Rs values close to 2.8 ohm/cm^2. The Rc values of both the S−C+(57.3 ohm/cm^2) and S+C−(50.2 ohm/cm^2) cells were relatively smaller than that of the TRG (388.2 ohm/cm^2) cell. Interestingly, TRG exhibits the highest Rc of 388.2 ohm/cm^2. This might be due to the apparent precipitation of the TRG solution during the dispersion of TRG electrodes. The Rp value of the TRG cell is large and out of scope for this measurement. It was found that the Rp values of the S−C+ and S+C− cells were 6.2 and 5.5 ohm/cm^2, respectively. Since both cells have the same composition materials, a similar Rp value was expected. Thus, the total internal resistance values of the S−C+ and S+C− cells were 66.3 and 58.5 ohm/cm^2, respectively.. As Rc represents the electron conduction of a cell, the Rc values of both the S−C+ and S+C− cells were selected to be as close as possible for the further charging–discharge comparison.

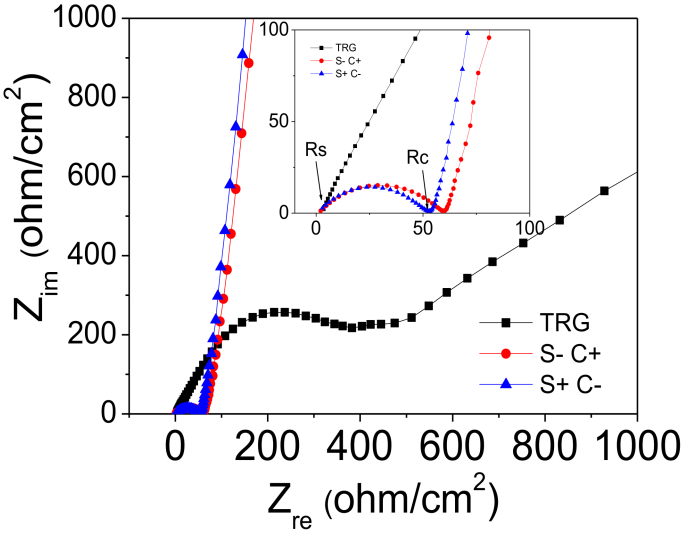

Figure 7. The impedance spectra of the TRG, S−C+ cell and S+C− cell.

Figure 8 plots the cyclic voltammetry (CV) curves of TRG, and the S−C+ and S+ C− cells. The cell current was measured in response to an applied voltage from 0 to 3.2 V. The accumulated charge (Q) with an applied voltage (V), follows Q = CV, where C is the capacitance. The response current follows I = C × dV/dt. For an ideal capacitance, such as for the S−C+ cell (Figure 8c), under a constant voltage

scan rate, a constant current should be observed resulting in a rectangular shape for the CV curve. However, we must consider that the capacitor is in series with an equivalent internal resistor (R = Rs + Rc + Rp) [27]. As with the TRG cell (Figure 8a), the charging or discharging current of the capacitor required a time constant (RC) to reach the steady state current [28]. With a large RC, it took more time to reach the steady state and, thus, it collapsed the rectangular profile of the current response in Figure 8a [29,30]. On the other hand, increasing the scan rate meant reducing the response time, which also caused collapsed results, as observed in Figure 8a–c. Figure 8d plots the capacitance against voltage profiles, in which the CV current at 100 mV/s was divided by the same scan rate. As can be seen, except for TRG, both S−C+ and S+C− cells showed a more rectangular-like capacitance response, indicating that they are closer to being ideal capacitors. The capacitance response of the cell was proportional to the accessible surface area for the IL electrolyte. In addition, these results suggested that the capacitance values of these cells were in the sequence of S−C+ > S+C− >TRG.

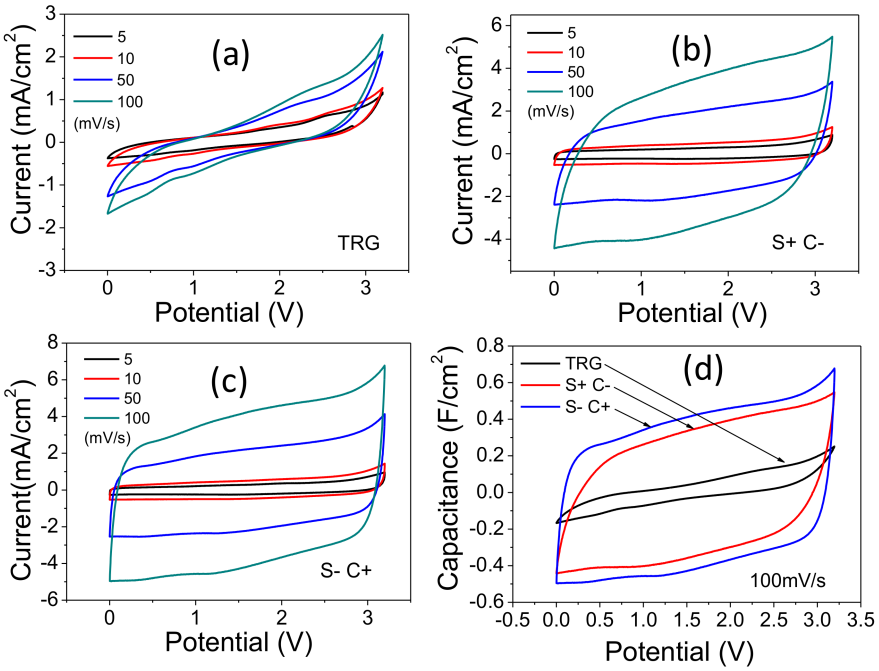

Figure 8. The cyclic voltammetry (CV) curves of (**a**) TRG, (**b**) S+C− and (**c**) S−C+ cells at the various voltage scan rates (**d**) comparison of the capacitance responses of the TRG, S+C− and S−C+ cells.

Due to the wide electrochemical window of EMI-TFSI, the operation voltage of all the cells could be operated at 3.2 V. Figure 9 plots the galvanostatic discharge currents vs. time of the TRG, S−C+ and S+C− cells As can be seen in Figure 9a, the voltage drop at the beginning of the discharging current is a result of voltage loss when the current across an equivalent resistance which is related to internal resistance R. Therefore, as expected TRG had the highest initial voltage drop among all the samples. The gravimetric specific capacitances (Cs) of the active materials on the electrodes were extracted from the gravimetric discharge curve, following [31–33]:

$$C_S = \frac{4C}{m} = \frac{4I\Delta t}{m\Delta V}$$

where m is the total weight of active materials on two electrodes, C is the capacitance of the cell, I is the constant current, Δt is the discharging time, and ΔV is the potential change (excluding the initial voltage drop) during discharging. Figure 10 plots the capacitance value deduced from the discharging current. As shown in the plot, all the capacitance responses decreased as a function of the specific current density. As the measured high current density was a result of the ions accumulated on the

electrode in a short period, the ions may not have had sufficient time to diffuse in and out of the deep region of the pores and, thus, reduced the accessible surface area, causing decreased capacitance [32]. Therefore, the value of the specific capacitance implies an accessible surface area at a specific current density. At a low current density (1 A/g), the capacitances of the S−C+(193.9 F/g) and S+C−(188.3 F/g) were much greater than that of TRG (43.1 F/g). This result indicates that the increased interlayer distances could increase the accessible surface area for the electrolyte. In the existing literature, most asymmetric supercapacitors are related to pseudocapacitors, which lead to a very large capacitance, which is greater than 200 F/g [34]. To the best of our knowledge, we are the first group to report surfactant intercalated asymmetric EDLC using ionic liquid electrolytes, resulting in a high capacitance of 193.9 F/g.

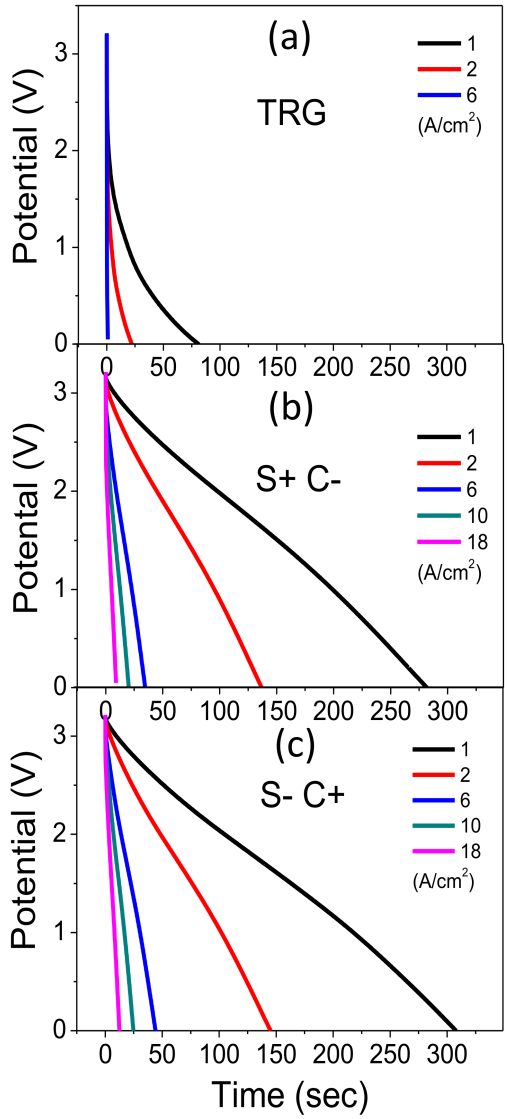

Figure 9. The discharge current vs. time of the (**a**) TRG, (**b**) S+C− and (**c**) S−C+ cells at various discharging currents.

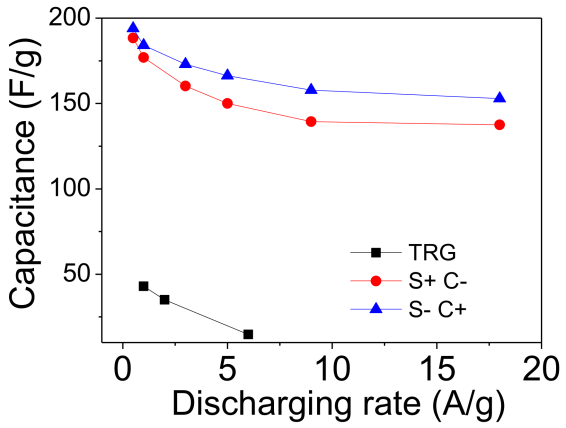

Figure 10. The capacitance density vs. current density of TRG, and the S+C− and S−C+ cells.

The energy density is obtained using the following equation [31–33].

$$E = 1/2\ CV^2 = 1/8\ Cs\ V^2$$

Moreover, the power density (P) is deduced according to [32,33]:

$$P = \frac{E}{\Delta t}$$

Figure 11 shows the Ragone plot which reveals the energy density of TRG, and the S+C− and S−C+ cells as a function of power density. Usually, energy density drops with power density as a result of voltage decay and capacitance reduction at a high power density. As can be seen, the significant initial voltage drop (Figure 9a) and the small capacitance (Figure 10) of the TRG cell resulted in its low energy density of 15.3 Wh/kg at 1 A/g. In contrast, the S−C+ and S+C− cells had similarily small voltage drops and large capacitances and, therefore, at 1 A/g, the S−C+ and S+C− cells had energy density values of 67.8 Wh/kg and 64.7 Wh/kg, respectively. Moreover, compared with the S−C+ asymmetric cell, the symmetric cell using TRGSE as both positive and negative electrodes, had a relatively lower energy density of 61.8 Wh/kg. However, with the increased current, the initial voltage drop of TRG became prominent and, thus, limited its energy density of 0.34 Wh/kg at 6 A/g. It was found that, at a current density of 18 A/g, the S−C+(36.8 Wh/kg) cell had a higher energy density retention compared to the S+C−(20.9 Wh/kg) cell, implying an intercalated ionic species effect on the performance of the EDLC cell.

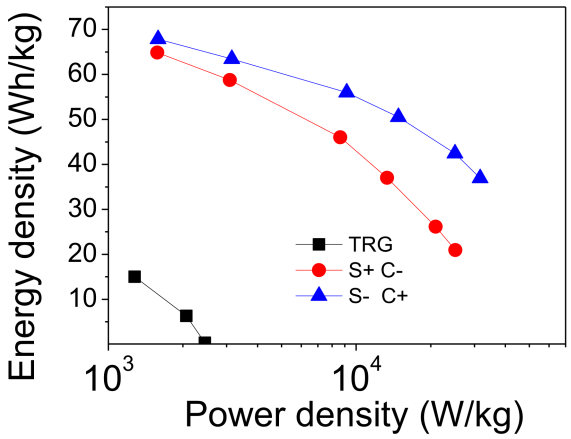

Figure 11. Ragone plot of the TRG, S+C− and S−C+ cells.

4. Conclusions

Ionic surfactants are employed to avoid the restacking of TRG sheets. A facile approach was used to tune the interlayer distance of the TRGSE and TRGCE composites through the Coulombic interaction between the intercalated surfactant and EMI-TFSI. The vibration modes of the intercalated surfactants were affected by the additional EMI-TFSI. In addition, the interlayer distance was enlarged from 0.36 nm to 3.92 nm, depending on the intercalated species, which suggests the formation of large-sized ionic aggregates or micelles between the composite sheets. The performance of the EDLC cells with asymmetric electrodes was evaluated. Due to the increased interlayer distance, at 1 A/g, the S−C+ cell had the highest energy density of 67.8 Wh/kg, which was 4.4-fold higher than that of the neat TRG cell. On the other hand, at 18 A/g, the S−C+(36.8 Wh/kg) cell still had a higher energy density than the S+C−(20.9 Wh/kg) cell. The observed results could be similar to the well-known proton transport in Nafion [35], as shown in Figure 2a. When the negative potential is applied to the (S−) electrode, the intercalated anionic surfactant may act as binding and release sites to facilitate the positive ions towards hopping to the TRG surface leading to the high capacitance and hence the high energy density of the S−C+ cell. In contrast, when the positive potential is applied to the (S+) electrode, the anionic sites may partially repel or screen the anions of electrolytes from accessing the TRG surface, resulting in the relatively-poor performance of the S+C− cell.

Acknowledgments: The authors acknowledge the financial support of the Ministry of Science and Technology (MOST 106-2221-E-151-037).

Author Contributions: Jun-Hong Lin, Bo-Wen Shi and Zhao-Cheng Chen conceived, designed and performed the experiments and also wrote the paper. The author read and approved the final manuscript.

Conflicts of Interest: The authors declare no conflicts of interest. The funding sponsors had no role in the design of the study, nor in the collection, analyses, or interpretation of data; nor in the writing of the manuscript; and had no role in the decision to publish the results.

References

1. Minakshi, M.; Mitchell, D.; Jones, R.; Alenazey, F.; Watcharatharapong, T.; Chakraborty, S.; Ahuja, R. Synthesis, structural and electrochemical properties of sodium nickel phosphate for energy storage devices. *Nanoscale* **2016**, *8*, 11291–11305. [CrossRef] [PubMed]
2. Ramkumar, R.; Minakshi, M. Fabrication of ultrathin $CoMoO_4$ nanosheets modified with chitosan and their improved performance in energy storage device. *Dalton Trans.* **2015**, *44*, 6158–6168. [CrossRef] [PubMed]
3. Lin, J.H.; Liu, Y.; Zhang, Q.M. Charge dynamics and bending actuation in Aquivion membrane swelled with ionic liquids. *Polymer* **2011**, *52*, 540–546. [CrossRef] [PubMed]
4. Liu, Y.; Zhao, R.; Ghaffari, M.; Lin, J.H.; Liu, S.; Cebeci, H.; de Villoria, G.R.; Montazami, R.; Wang, D.; Wardle, B.L.; et al. Equivalent circuit modeling of ionomer and ionic polymer conductive network composite actuators containing ionic liquids. *Sens. Actuators A Phys.* **2012**, *181*, 70–76. [CrossRef]
5. Liu, Y.; Lu, C.Y.; Twigg, S.; Ghaffari, M.; Lin, J.H.; Winograd, N.; Zhang, Q.M. Direct Observation of Ion Distributions near Electrodes in Ionic Polymer Actuators Containing Ionic Liquids. *Sci. Rep.* **2013**, *3*, 973. [CrossRef] [PubMed]
6. Liu, Y.; Liu, S.; Lin, J.H.; Wang, D.; Jain, V.; Montazami, R.; Heflin, J.R.; Li, J.; Madsen, L.; Zhang, Q.M. Ion transport and storage of ionic liquids in ionic polymer conductor network composites. *Appl. Phys. Lett.* **2010**, *96*. [CrossRef]
7. Galinski, M.; Lewandowski, A.; Stepniak, I. Ionic liquids as electrolytes. *Electrochim. Acta* **2006**, *51*, 5567–5580. [CrossRef]
8. Zhang, Y.; Feng, H.; Wu, X.B.; Wang, L.Z.; Zhang, A.Q.; Xia, T.C.; Dong, H.C.; Li, X.F.; Zhang, L.S. Progress of electrochemical capacitor electrode materials: A review. *Int. J. Hydrogen Energy* **2009**, *34*, 4889–4899. [CrossRef]
9. Stankovich, S.; Dikin, D.A.; Piner, R.D.; Kohlhaas, K.A.; Kleinhammes, A.; Jia, Y.; Wu, Y.; Nguyen, S.T.; Ruoff, R.S. Synthesis of graphene-based nanosheets via chemical reduction of exfoliated graphite oxide. *Carbon* **2007**, *45*, 1558–1565. [CrossRef]

10. Tan, C.L.; Cao, X.H.; Wu, X.J.; He, Q.Y.; Yang, J.; Zhang, X.; Chen, J.; Zhao, W.; Han, S.; Nam, G.-H.; et al. Recent Advances in Ultrathin Two-Dimensional Nanomaterials. *Chem. Rev.* **2017**, *117*, 6225–6331. [CrossRef] [PubMed]
11. Zhu, Y.W.; Murali, S.; Cai, W.W.; Li, X.S.; Suk, J.W.; Potts, J.R.; Ruoff, R.S. Graphene and Graphene Oxide: Synthesis, Properties, and Applications. *Adv. Mater.* **2010**, *22*, 3906–3924. [CrossRef] [PubMed]
12. Fouda, A.N.; Abu Assy, M.K.; El Enany, G.; Yousf, N. Enhanced Capacitance of Thermally Reduced Hexagonal Graphene Oxide for High Performance Supercapacitor. *Fuller. Nanotub. Carbon Nanostruct.* **2015**, *23*, 618–622. [CrossRef]
13. Kim, B.C.; Cho, W.J.; Lee, W.G.; Kim, S.J.; Jalili, R.; Park, S.Y.; Wallace, G.G.; Yu, K.H.; Chang, S.-J. Capacitive behaviour of thermally reduced graphene oxide in a novel ionic liquid containing di-cationic charge. *Synth. Metals* **2014**, *193*, 110–116. [CrossRef]
14. Mao, L.; Zhang, K.; Chan, H.S.O.; Wu, J.S. Surfactant-stabilized graphene/polyaniline nanofiber composites for high performance supercapacitor electrode. *J. Mater. Chem.* **2012**, *22*, 80–85. [CrossRef]
15. Zhang, K.; Mao, L.; Zhang, L.L.; Chan, H.S.O.; Zhao, X.S.; Wu, J.S. Surfactant-intercalated, chemically reduced graphene oxide for high performance supercapacitor electrodes. *J. Mater. Chem.* **2011**, *21*, 7302–7307. [CrossRef]
16. Sundaram, M.M.; Mitchell, D.R.G. Dispersion of Ni^{2+} ions via acetate precursor in the preparation of NaNiPO4 nanoparticles: Effect of acetate vs. nitrate on the capacitive energy storage properties. *Dalton Trans.* **2017**, *46*, 13704–13713. [CrossRef] [PubMed]
17. Largeot, C.; Portet, C.; Chmiola, J.; Taberna, P.L.; Gogotsi, Y.; Simon, P. Relation between the ion size and pore size for an electric double-layer capacitor. *J. Am. Chem. Soc.* **2008**, *130*, 2730–2731. [CrossRef] [PubMed]
18. Marcano, D.C.; Kosynkin, D.V.; Berlin, J.M.; Sinitskii, A.; Sun, Z.Z.; Slesarev, A.; Alemany, L.B.; Lu, W.; Tour, J.M. Improved Synthesis of Graphene Oxide. *ACS Nano* **2010**, *4*, 4806–4814. [CrossRef] [PubMed]
19. Ramimoghadam, D.; Hussein, M.Z.B.; Taufiq-Yap, Y.H. The Effect of Sodium Dodecyl Sulfate (SDS) and Cetyltrimethylammonium Bromide (CTAB) on the Properties of ZnO Synthesized by Hydrothermal Method. *Int. J. Mol. Sci.* **2012**, *13*, 13275–13293. [CrossRef] [PubMed]
20. Sau, T.K.; Murphy, C.J. Self-assembly patterns formed upon solvent evaporation of aqueous cetyltrimethylammonium bromide-coated gold nanoparticles of various shapes. *Langmuir* **2005**, *21*, 2923–2929. [CrossRef] [PubMed]
21. Suteewong, T.; Sai, H.; Lee, J.; Bradbury, M.; Hyeon, T.; Gruner, S.M.; Wiesner, U. Ordered mesoporous silica nanoparticles with and without embedded iron oxide nanoparticles: Structure evolution during synthesis. *J. Mater. Chem.* **2010**, *20*, 7807–7814. [CrossRef]
22. Taberna, P.L.; Simon, P.; Fauvarque, J.F. Electrochemical characteristics and impedance spectroscopy studies of carbon-carbon supercapacitors. *J. Electrochem. Soc.* **2003**, *150*, A292–A300. [CrossRef]
23. Lewandowski, A.; Olejniczak, A.; Galinski, M.; Stepniak, I. Performance of carbon-carbon supercapacitors based on organic, aqueous and ionic liquid electrolytes. *J. Power Sources* **2010**, *195*, 5814–5819. [CrossRef]
24. Kotz, R.; Carlen, M. Principles and applications of electrochemical capacitors. *Electrochim. Acta* **2000**, *45*, 2483–2498. [CrossRef]
25. Pandey, G.P.; Rastogi, A.C. Solid-State Supercapacitors Based on Pulse Polymerized Poly(3,4-ethylenedioxythiophene) Electrodes and Ionic Liquid Gel Polymer Electrolyte. *J. Electrochem. Soc.* **2012**, *159*, A1664–A1671. [CrossRef]
26. Liu, R.; Cho, S.I.; Lee, S.B. Poly(3,4-ethylenedioxythiophene) nanotubes as electrode materials for a high-powered supercapacitor. *Nanotechnology* **2008**, *19*. [CrossRef] [PubMed]
27. Samal, R.; Dash, B.; Sarangi, C.K.; Sanjay, K.; Subbaiah, T.; Senanayake, G.; Minakshi, M. Influence of Synthesis Temperature on the Growth and Surface Morphology of Co_3O_4 Nanocubes for Supercapacitor Applications. *Nanomaterials* **2017**, *7*, 356. [CrossRef] [PubMed]
28. Yoon, S.; Lee, J.W.; Hyeon, T.; Oh, S.M. Electric double-layer capacitor performance of a new mesoporous carbon. *J. Electrochem. Soc.* **2000**, *147*, 2507–2512. [CrossRef]
29. Mo, Y.F.; Wan, Y.F.; Chau, A.; Huang, F.C. Graphene/Ionic Liquid Composite Films and Ion Exchange. *Sci. Rep.* **2014**, *4*, 5466. [CrossRef] [PubMed]
30. Du, M.; Yang, T.; Ma, S.Y.; Zhao, C.Z.; Jiao, K. Ionic liquid-functionalized graphene as modifier for electrochemical and electrocatalytic improvement: Comparison of different carbon electrodes. *Anal. Chim. Acta* **2011**, *690*, 169–174. [CrossRef] [PubMed]

31. Zhu, Y.W.; Murali, S.; Stoller, M.D.; Ganesh, K.J.; Cai, W.W.; Ferreira, P.J.; Pirkle, A.; Wallace, R.M.; Cychosz, K.A.; Thommes, M.; et al. Carbon-Based Supercapacitors Produced by Activation of Graphene. *Science* **2011**, *332*, 1537–1541. [CrossRef] [PubMed]
32. Tamilarasan, P.; Ramaprabhu, S. Graphene based all-solid-state supercapacitors with ionic liquid incorporated polyacrylonitrile electrolyte. *Energy* **2013**, *51*, 374–381. [CrossRef]
33. Yang, H.; Kannappan, S.; Pandian, A.S.; Jang, J.H.; Lee, Y.S.; Lu, W. Graphene supercapacitor with both high power and energy density. *Nanotechnology* **2017**, *28*. [CrossRef] [PubMed]
34. Iamprasertkun, P.; Krittayavathananon, A.; Seubsai, A.; Chanlek, N.; Kidkhunthod, P.; Sangthong, W.; Maensiri, S.; Yimnirun, R.; Nilmoung, S.; Pannopard, P.; et al. Charge storage mechanisms of manganese oxide nanosheets and N-doped reduced graphene oxide aerogel for high-performance asymmetric supercapacitors. *Sci. Rep.* **2016**, *6*, 12. [CrossRef] [PubMed]
35. He, X.Y.; He, G.W.; Zhao, A.Q.; Wang, F.; Mao, X.L.; Yin, Y.H.; Cao, L.; Zhang, B.; Wu, H.; Jiang, Z. Facilitating Proton Transport in Nafion-Based Membranes at Low Humidity by Incorporating Multifunctional Graphene Oxide Nanosheets. *ACS Appl. Mater. Interfaces* **2017**, *9*, 27676–27687. [CrossRef] [PubMed]